Article Type: Full Paper

Understanding the Role of Cesium and Rubidium Additives in Perovskite Solar Cells: Trap States, Charge Transport and Recombination

Yinghong Hu,[1] Eline M. Hutter,[2] Philipp Rieder,[3] Irene Grill,[1] Jonas Hanisch,[4] Meltem F. Aygüler,[1] Alexander G. Hufnagel,[1] Matthias Handloser,[5] Thomas Bein,[1] Achim Hartschuh,[1] Kristofer Tvingstedt,[3] Vladimir Dyakonov,[3] Andreas Baumann,[6,] Tom J. Savenije,[2,*] Michiel L. Petrus,[1,*] Pablo Docampo.[7,*]*

[1] Department of Chemistry and Center for NanoScience (CeNS), LMU Munich, Butenandtstr. 11, 81377 Munich, Germany

[2] Department of Chemical Engineering, Delft University of Technology, van der Maasweg 9, 2629 HZ Delft, The Netherlands

[3] Experimental Physics VI, Julius Maximillian University of Würzburg, 97074 Würzburg, Germany

[4] Zentrum für Sonnenenergie- und Wasserstoff-Forschung (ZSW) Baden-Württemberg, Meitnerstr. 1, 70563 Stuttgart, Germany

[5] TOPTICA Photonics AG, Lochhamer Schlag 19, 81266 Gräfelfing, Germany

[6] Bavarian Center for Applied Energy Research, Magdalene-Schoch-Str. 3, 97074 Würzburg, Germany

[7] Physics Department, School of Electrical and Electronic Engineering, Newcastle University, Merz Court, Newcastle upon Tyne, NE1 7RU, United Kingdom

Email: Pablo.Docampo@newcastle.ac.uk, Michiel.Petrus@lmu.de, T.J.Savenije@TUDelft.nl, Andreas.Baumann@zae-bayern.de,

Keywords

perovskite solar cell, inorganic cations, trap density, charge carrier mobility, charge recombination

Abstract

Adding cesium (Cs) and rubidium (Rb) cations to $FA_{0.83}MA_{0.17}Pb(I_{0.83}Br_{0.17})_3$ hybrid lead halide perovskites results in a remarkable improvement in solar cell performance, but the origin of the enhancement has not been fully understood yet. In this work, Time-of-Flight (ToF), Time-Resolved Microwave Conductivity (TRMC), and Thermally Stimulated Current (TSC) measurements were performed to elucidate the impact of the inorganic cation additives on the trap landscape and charge transport properties within perovskite solar cells. These complementary techniques allow for the assessment of both local features within the perovskite crystals and macroscopic properties of films and full devices. Strikingly, Cs-incorporation was shown to reduce the trap density and charge recombination rates in the perovskite layer. This is consistent with the significant improvements in the open-circuit voltage and fill factor of Cs-containing devices. By comparison, Rb-addition results in an increased charge carrier mobility, which is accompanied by a minor increase in device efficiency and reduced current-voltage hysteresis. By mixing Cs and Rb in quadruple cation (Cs–Rb–FA–MA) perovskites, the advantages of both inorganic cations can be combined. Our study provides valuable insights into the role of these additives in multiple-cation perovskite solar cells, which are essential for the design of high-performance devices.

1. Introduction

In the past few years, hybrid lead halide perovskites established themselves as outstanding materials for photovoltaic (PV) applications. Recently, inorganic cations such as rubidium (Rb) and cesium (Cs) have been added to the perovskite, resulting in a boost in the power conversion efficiency (PCE) up to 21.6%.[1] The state-of-the-art perovskite solar cells comprise a multi-cation mixed-halide hybrid perovskite and show impressive stabilized power output under working conditions.[1, 2] The inorganic cation additives have been shown to improve the phase stability of the photoactive formamidinium lead iodide ($FAPbI_3$) perovskite layer by suppressing the phase transition into the yellow non-perovskite structure at room temperature.[3-7] However, the stabilization of the black perovskite phase is based on fine-tuning the Goldschmidt tolerance factor, which can also be achieved by incorporation of smaller methylammonium (MA) cations into the formamidinium (FA)-dominated perovskite structure, without the need for the even smaller Cs or Rb cations.[8, 9] It is likely that the inorganic cation additives do not only stabilize the crystal structure, but also have a strong impact on the optoelectronic properties of the perovskite, leading to the observed enhancement in solar cell performance.

In order to reach record efficiencies and high stability, extensive device optimization work with a strong focus on the processing of the perovskite layer has been performed. Various combinations and ratios between the monovalent cations (FA, MA, Cs and Rb) and the halides (I and Br) have been explored and optimized along with different perovskite fabrication processes.[3-6, 9-15] However, the origin of the increased device performance that has been demonstrated for Rb- and Cs-containing perovskite solar cells remains rather unclear. In order to engineer perovskite

solar cells with the highest possible device performance and stability, it is essential to understand the impact of the inorganic cation additives on the perovskite's optoelectronic properties.

In this work, we investigate the effect of Cs- and Rb-addition on the electronic landscape and the charge transport properties of the multiple-cation mixed-halide perovskite $FA_{0.83}MA_{0.17}Pb(I_{0.83}Br_{0.17})_3$ in state-of-the-art perovskite solar cells. We combine three complementary probing techniques: Time-of-Flight (ToF), Time-resolved Microwave Conductivity (TRMC) and Thermally Stimulated Current (TSC) measurements. Our results indicate that Cs markedly reduces the trap density, as well as the second order recombination rate of free mobile charges in the perovskite bulk material. Furthermore, the trap states in Cs-containing perovskites appear to be shallower than in non-modified perovskite devices. These improvements are in good agreement with a notable enhancement of device performance employing Cs-containing perovskites. By comparison, our results show that Rb-addition increases the charge carrier mobility, but that it has only a minor impact on the trap landscape within the perovskite solar cell and results in marginal improvements in device performance. Nevertheless, Rb reduces current–voltage hysteresis and leads to a more stabilized power output. After clarifying the individual role of each inorganic cation additive, the benefits of both Cs and Rb-addition can be found in quadruple cation (Cs –Rb–FA–MA) perovskites.

2. Results

2.1. Solar Cell Performance

We investigated the influence of Rb and Cs cations as additives on the PV performance of planar perovskite solar cells with the following device architecture: glass/fluorinated tin oxide (FTO)/compact TiO_2/perovskite/Spiro-OMeTAD/Au. According to a protocol reported by Saliba *et al*.[1], we synthesized the multi-cation mixed-halide $(FA_{0.83}MA_{0.17})Pb(I_{0.83}Br_{0.17})_3$ perovskite (FAMA), and added approximately 5 mol% of RbI, CsI or a combination of both to the FAMA precursor solution. The resulting samples are denoted in the following as Rb5, Cs5 and Rb5Cs5, i.e. Rb5 means that 5 mol% of Rb cations were added. Our previous XRD results show that the Cs is fully incorporated into the perovskite lattice, while the same amount of Rb preferentially forms a $RbPb(I_{1-x}Br_x)_3$ side phase.[16] The current–voltage (*J*–*V*) characteristics of at least 17 cells were evaluated for each type of perovskite layer under one sun illumination according to air mass 1.5 global (AM1.5G) radiation. Further details regarding the device preparation and characterization are given in the Supporting Information. **Figure 1** shows the schematic representation of the layered device architecture, the stabilized output under maximum power conditions at AM1.5G sun illumination, as well as the distribution of the PV device parameters for FAMA, Rb5, Cs5 and Rb5Cs5 solar cells. Representative *J*–*V* curves of champion cells are shown in Figure S1 in the Supporting Information. Scanning Electron Microscopy (SEM) cross-section images of the full devices are depicted in Figure S2.

In accordance with previous reports, we find that the PV performance is substantially enhanced for Cs5 devices compared to plain FAMA-based devices.[2] The enhancement in power conversion

efficiency upon CsI addition can be ascribed to a significant improvement in all solar cell parameters (Figure 1c–f), i.e. short-circuit current (J_{sc}), open-circuit voltage (V_{oc}) and fill factor (FF). The addition of RbI only leads to minor improvements in J_{sc}, V_{oc} and FF in the corresponding Rb5 device. When both Rb and Cs cations were used as additives, the resulting Rb5Cs5 devices show a comparable PV performance to that of the Cs5 devices. However, the presence of Rb results in a more narrow distribution of the Rb5Cs5 device performance parameters, indicating higher reproducibility. Moreover, the presence of Rb in the Rb5Cs5 perovskite film leads to the highest stabilized power output under constant illumination over 300 s (Figure 1b) which is superior to that of Cs5 and is in agreement with literature reports.[1, 2] Similar trends regarding J_{sc}, V_{oc} and stabilized power output were also observed for devices prepared on compact SnO_x films instead of TiO_2 serving as electron transport layers (Figure S3–4).

The increase in J_{sc} upon addition of the inorganic cations is most likely related to the formation of a larger volume percentage of photoactive material through the reaction between the CsI or RbI additive and the excess of PbI_2 which is present in the non-stoichiometric FAMA solution. The excess PbI_2 was intentionally added to the perovskite precursor solution due to its potential passivation effect in perovskite solar cells, which is a standard procedure for the highest performing solar cells described in the literature.[1, 2, 17-19] By reacting the PbI_2 excess with the CsI or RbI additive, the absorptance of the resulting perovskite film increases (Figure S5). Furthermore, external quantum efficiency (EQE) measurements were conducted and the measured integrated current densities are in close agreement with the J_{sc} values obtained from the *J*–*V* curves (Figure S6). The EQE data demonstrate an increase of ~4% in current density when 5% of Rb or Cs are added and overall, Rb5Cs5 leads to the highest current densities. We point out

that the reduction of excess PbI_2 in the perovskite layer upon inorganic cation addition is not the origin of the observed PCE improvements. This is supported by comparing FAMA devices with 0%, 5% and 10% PbI_2 excess which show very similar photovoltaic performance (Figure S7). In order to elucidate the origin of the V_{oc} and FF improvement in perovskite solar cells upon Cs- and/or Rb-addition, we thoroughly investigated the change in charge carrier mobility, charge recombination rates and trap densities of the perovskite thin films.

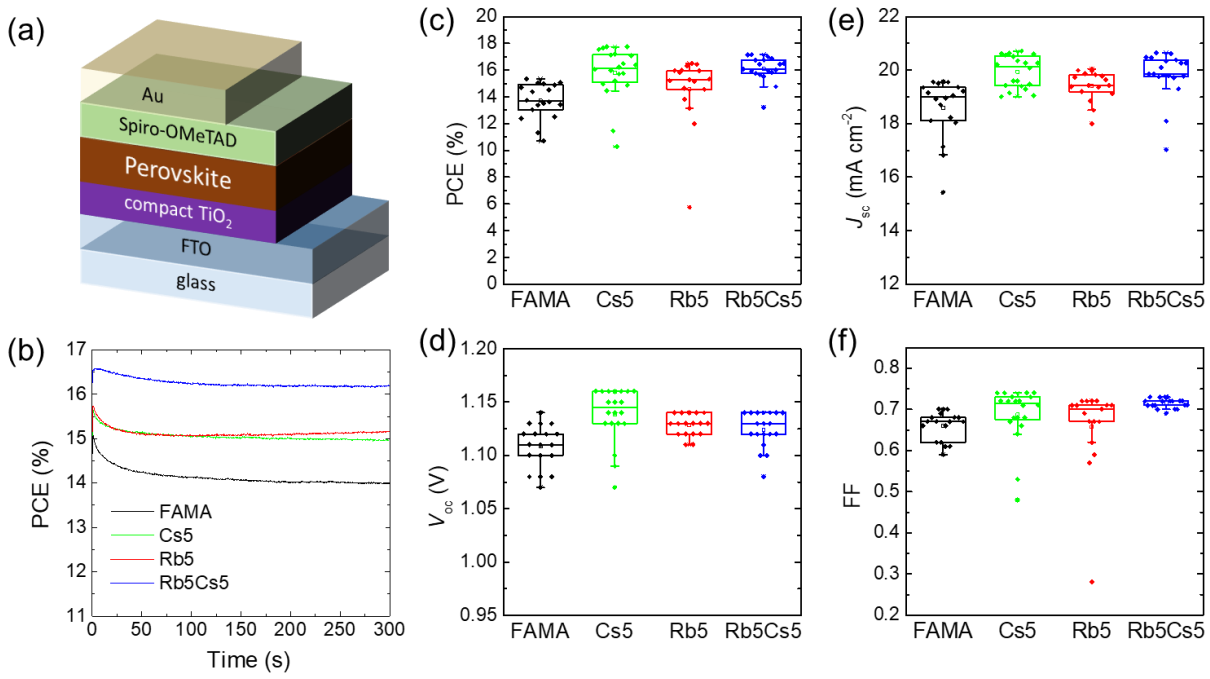

Figure 1. a) Schematic representation of the device architecture of the perovskite solar cells. b) Maximum power point tracking for encapsulated perovskite solar cells under constant 1 sun AM1.5G illumination measured in air. c)–f) Box chart representation of photovoltaic parameters of perovskite solar cells under simulated AM1.5G sunlight. The current-voltage (*J*–*V*) curve of at least 17 cells for each type of perovskite layer were recorded at a scan rate of 0.1 V s^{-1}.

2.2. Charge Carrier Transport

2.2.1. Macroscopic Charge Carrier Transport (Time-of-Flight Measurements)

To probe the impact of the Cs and Rb addition on charge carrier transport in the perovskite absorber, we performed Time-of-Flight (ToF) measurements on laterally contacted perovskite layers.[20] Further information about the experimental setup and the procedure of the transient photocurrent measurements is given in the Supporting Information (Figure S8).

We generate charge carriers in the perovskite layer by illumination using pulsed laser excitation (λ = 510 nm) close to one of the gold electrodes. By simultaneously applying a constant external electric field of 5 kV cm^{-1} (for only a few hundreds of milliseconds to mitigate the effect of ionic migration), the photo-generated charge carriers (either electrons or holes) move across the film within the gap towards the opposite Au electrode. The resulting photocurrent transients show that the transit time t_{tr} that is required for charge carriers to travel laterally from the excitation spot to the opposite Au contact increases with increasing electrode distances (Figure S9). A previously reported procedure[20] was employed to extract the transit time from the measured photocurrent transient. The average charge carrier mobility μ in the perovskite films can be approximated by the ToF equation:

$$\mu = \frac{d}{E \cdot t_{tr}} \qquad (1)$$

with d as the inter-electrode distance, $E = U_{bias}/d$ the applied electric field and t_{tr} the ToF transit time. By plotting t_{tr} against d, the slope of the linear regression in **Figure 2** is a direct measure for the mobility since the applied electric field was identical for all perovskite films. Depending on the polarity of the applied electric field, holes or electrons can be probed as the mobile species since charges are locally generated near one electrode. Therefore, the mobility of holes (μ_h) or electrons (μ_e) can be differentiated using the ToF technique.

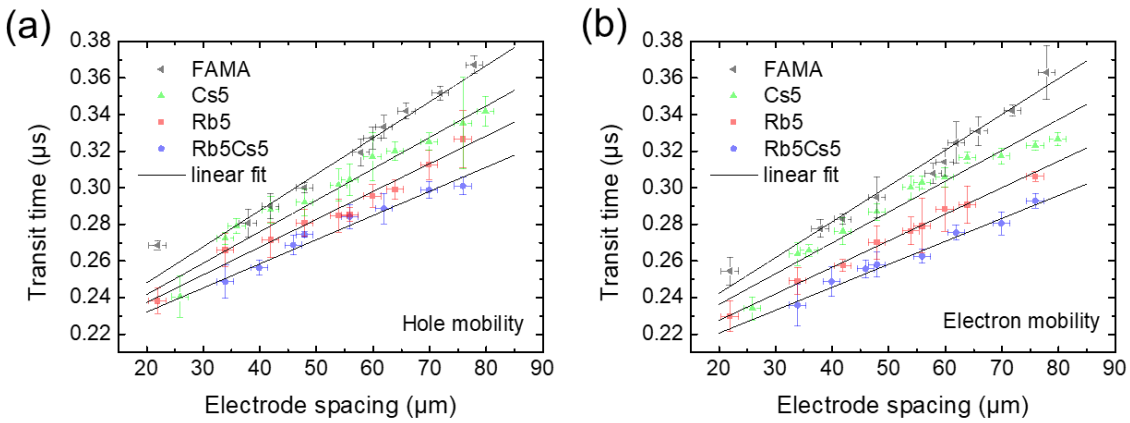

Figure 2. Determination of charge carrier mobilities in perovskite thin films using the ToF technique. Extracted transit times (t_{tr}) as a function of electrode distance *d* under a) positive bias to extract hole mobility μ_h and b) negative bias to extract electron mobility μ_e. The value for charge carrier mobility can be derived from the slope of the linear fits and are listed in Table 1.

Table 1. Charge carrier mobility of perovskite thin films determined by ToF measurements.

	μ_h (cm^2 V^{-1}s^{-1})	μ_e (cm^2 V^{-1}s^{-1})	$\mu_{sum,ToF}$ (cm^2 V^{-1}s^{-1})
FAMA	10	10	20
Cs5	11	12	23
Rb5	13	14	27
Rb5Cs5	15	16	31

Table 1 shows the charge carrier mobilities for the different perovskite films calculated from the regression slopes in Figure 2. In addition to the individual charge carrier mobility values, the sum of both electron and hole mobility $\mu_{sum,\ ToF}$ is also provided. Strikingly, all samples exhibit very similar mobility values for holes and electrons, indicating highly balanced charge transport over distances of at least 80 µm (maximum size of the in-plane electrode spacings). In comparison to the sum of mobility for FAMA ($\mu_{sum,ToF}$ = 20 cm^2 V^{-1}s^{-1}), Cs5 shows slightly increased mobilities

($\mu_{sum,ToF}$ = 23 $cm^2 V^{-1}s^{-1}$), while a stronger increase was found for Rb5 ($\mu_{sum,ToF}$ = 27 $cm^2 V^{-1}s^{-1}$). In particular, the combination of Rb and Cs as additives leads to a perovskite layer with mobility values reaching 31 $cm^2 V^{-1}s^{-1}$, which corresponds to a ~50% improvement compared to FAMA.

In our ToF experiments, charge carriers need to travel laterally across various grain boundaries to the opposite electrode to generate a measureable photocurrent. Grain boundaries have been reported to include a high density of defect sites, leading to charge recombination and reduced photocurrent.[20, 21] SEM top-view images of the perovskite films show comparable crystal morphologies and grain sizes of 200–500 nm for FAMA, Cs5, Rb5 and Rb5Cs5 (Figure S10). Therefore, the observed increase in mobility through the addition of Rb and Cs to the perovskite precursor mixture cannot be soley ascribed to a lower density of grain boundaries within the probed distances. Nevertheless, it is possible that the inorganic cation additives (especially Rb) influence the barrier properties of the grain boundaries inside the perovskite layer, thereby improving inter-grain charge transport, which may result in higher mobility values. Regarding device efficiency, the lower mobility of Cs5 compared to Rb5 does not explain why Cs shows a larger PCE enhancement than Rb alone. Hence, it is necessary to investigate the change in trap density and recombination rates within the perovskite layer upon addition of the inorganic cations.

2.2.2. Microscopic Charge Carrier Transport (Time-Resolved Microwave Conductivity Measurements)

Further insight into the relationship between the addition of Cs and/or Rb to the FAMA perovskite and the associated mobilities and lifetimes of free charges can be gained through Time-Resolved Microwave Conductivity (TRMC) measurements. TRMC traces were measured at different light intensities and fitted according to a kinetic model to extract the trap densities and rate constants for second order recombination.[22, 23] In **Figure 3**, the intensity-normalized photoconductance transients are plotted for the various bare perovskite samples on quartz substrates as a function of time after excitation at 650 nm. Typically, on pulsed excitation the photoconductance sharply rises as a result of the photo-generation of mobile charge carriers, which is followed by a decay due to charge recombination and/or immobilization of charge carriers in trap states. For all perovskite materials studied, we observe a gradual reduction in the charge carrier lifetime when increasing the laser intensity, which is characteristic for higher order recombination.[22]

Analogous to our previous work,[22, 24] we used a kinetic model to obtain quantitative information from the intensity-dependent TRMC traces. This kinetic model (see Figure S11) takes into account the generation of electrons and holes and their recombination via second order band–to–band recombination (k_2) or trap-assisted recombination, which will dominate when the charge carrier density is lower than the trap density N_T. Details on the fitting procedure can be found in the Supporting Information. As shown in Figure 3 by the dotted lines, excellent agreement is obtained between the modelled and the experimental TRMC traces. The rate constants for trap filling (k_T) and trap emptying (k_D) are modelled to be 1.0×10^{-9} cm^{-3} s^{-1} and 9.0×10^{-10} cm^{-3} s^{-1}, respectively, for all perovskite samples.The extracted values for trap densities, second order recombination rates and effective mobilities are summarized in **Table 2**.

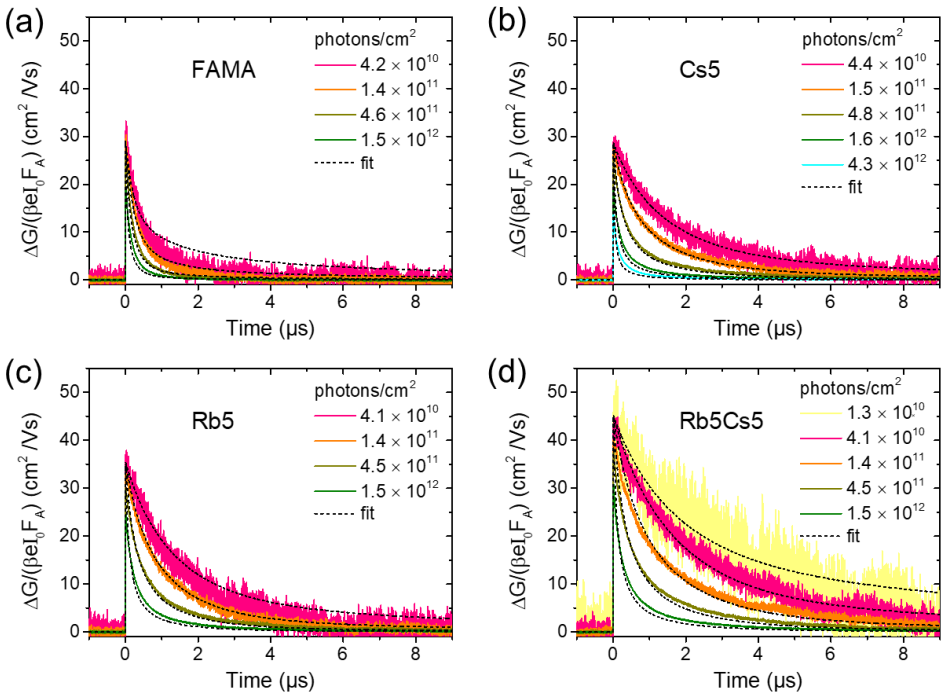

Figure 3. Time-resolved microwave conductivity (TRMC) traces recorded for different perovskites on quartz substrates. a) FAMA, b) Cs5, c) Rb5 and d) Rb5Cs5. The dotted black lines indicate the corresponding fits to the TRMC traces according to our kinetic model.

Table 2. Kinetic parameters for the recombination process, trapping and effective mobilities assessed by TRMC.

Sample	Second order recombination rate constant (k_2) [$cm^{-3}s^{-1}$]	Trap density ($N_{T,TRMC}$) [cm^{-3}]	Effective mobility (μ_{TRMC}) [$cm^2\ V^{-1}s^{-1}$]
FAMA	6.0×10^{-10}	2.5×10^{15}	42
Cs5	4.2×10^{-10}	8.0×10^{14}	40
Rb5	3.5×10^{-10}	1.0×10^{15}	50
Rb5Cs5	3.0×10^{-10}	8.0×10^{14}	62

The FAMA and Cs5 perovskite films show relatively high local charge carrier mobilities (μ_{TRMC}) exceeding 40 $cm^2 V^{-1}s^{-1}$. More importantly, a further improvement in charge carrier mobility can be found in Rb5 and, especially in Rb5Cs5 (μ_{TRMC} > 60 $cm^2 V^{-1}s^{-1}$). Here we note that for TRMC measurements, the sum of both the electron and hole mobility is obtained from the signal.[22] Thus, the mobility values extracted from TRMC need to be compared with the sum of electron and hole mobility values $\mu_{sum,ToF}$ obtained from ToF (see Table 1). It is truly remarkable that the charge carrier mobilities as determined from TRMC and from ToF follow almost exactly the same trend. From this resemblance we can conclude that the Rb introduction leads to a definite increase of the charge carrier mobility.

Furthermore, it is noteworthy that the second order recombination rate, k_2, is also reduced by the presence of the inorganic cation additives, Rb and Cs. Similarly to the improvement of charge carrier mobility, the reduction of the second order recombination rate constant is most pronounced in Rb5Cs5 and thus significantly extends the charge carrier lifetimes throughout the full range of excitation densities shown in Figure 3. An increase in charge carrier lifetime is also confirmed by time-resolved photoluminescence (PL) measurements, indicated by the prolonged PL lifetime in Cs5, Rb5 and Rb5Cs5 compared to FAMA (Figure S12). These observations show that the addition of Cs and Rb favorably slows down the effective second order band-to-band (electron-hole) recombination within the perovskite bulk material, which could explain the increased V_{oc} of the corresponding devices.

Both the change in k_2 and in μ_{TRMC} might be linked to alterations in the band structure of the perovskite compound, induced by the presence of the inorganic cations. Additionally, we note

that the effective second order recombination rate in metal halide perovskite comprises both radiative and non-radiative processes.[25, 26] For instance, increasing radiative recombination could significantly enhance the charge carrier lifetime via reabsorption events.[27] Alternatively, since changing the cations (locally) affects the distances between the lead halide octahedra and their tilting angles, the retarded second order recombination in the presence of Rb and/or Cs could also be due to changes in the band structure.

The performance of perovskite solar cells is also related to the presence of trap states, which can act as recombination pathways for photo-generated charge carriers. Our TRMC results indicate a trap density of approximately $N_{T,TRMC} = 2.5 \times 10^{15}$ cm^{-3} in the FAMA perovskite sample. Interestingly, the introduction of Cs substantially reduces the trap density ($N_{T,TRMC} = 8.0 \times 10^{14}$ cm^{-3}), i.e. by a factor of three compared to the FAMA perovskite film, in line with the observed enhancement in the device performance for Cs5. When only Rb is added to the perovskite precursor solution, the resulting Rb5 film also reveals a lower trap density as compared to FAMA ($N_{T,TRMC} = 1.0 \times 10^{15}$ cm^{-3}). However, the effect is smaller than for Cs-incorporation. When both Cs and Rb are introduced as in Rb5Cs5, the trap density is comparable to the Cs5 sample, showing the same trend observed for the PCE values.

Our TRMC results thus suggest that the notable improvement of device performance in Cs5 and Rb5Cs5 cannot be simply assigned to an increase in mobility, but rather to a decrease of effective second order recombination rate as well as a lower trap density compared to FAMA. In order to obtain further insights into the amount and the energetic levels of these suggested trap states, we conducted Thermally Stimulated Current (TSC) experiments on complete solar cells.

2.3. Defect Spectroscopy (Thermally Stimulated Current Measurements)

As an electrically sensitive technique, TSC allows for the investigation of whole devices, thus linking changes in the trap states to the respective device performance. The TSC measurements were conducted on complete solar cells differing only in the photoactive layer, which was one of the four perovskite types: FAMA, Cs5, Rb5 or Rb5Cs5. To obtain the TSC spectra, the devices were cooled to a temperature well below the activation energy of the investigated trap states (here: 30 K) in the dark. Subsequently, the trap states were optically filled via illumination with a cold LED array. In order to release the previously trapped charge carriers within the devices, the solar cells were gradually heated up to 300 K at a constant rate of 3 K min^{-1}. Further details regarding the TSC technique have been reported earlier by Baumann *et al*.[28] The respective TSC spectra for each solar cell are shown in

Figure 4a.

For the pure FAMA based device, a very wide TSC signal can be identified, indicating a broad distribution of trap state energies within the device. Our results show that the exclusive addition of Rb to the FAMA precursor solution (Rb5) has only a negligible impact on the overall TSC signal intensity and shape. However, the introduction of Cs into the perovskite film (Cs5, Rb5Cs5) considerably reduces the TSC signal, indicating an overall reduction of the trap density. Instead of a broad TSC peak, a more distinct peak is visible at around 230–240 K for both Cs-containing systems. We can assess the depth of these trap states by estimating the activation energy of the trap states. Herein, the so-called initial rise method is used according to the equation:[29, 30]

$$I_{TSC} \propto exp\left(-\frac{E_A}{k_B T}\right) \quad (2)$$

where k_B is the Boltzmann constant and T the temperature, at which the TSC signal I_{TSC} starts to rise. The data range used to fit the initial rise is denoted in the corresponding Arrhenius plot of the TSC spectra in

Figure 4b as T1, T2 and T3. **Table 3** shows a summary of the activation energies of trap states for the devices with different perovskite absorber layers.

For the FAMA based device, trap states with an activation energy of $E_{A,T1,FAMA}$= 248 meV are found (T1). With a slightly higher activation energy of $E_{A,T1,Rb5}$= 283 meV, the trap states appear to shift even deeper into the bandgap with the small amount of Rb added to the perovskite layer (Rb5). In contrast, the opposite behavior is found for the introduction of Cs, where the energetic depth of the deepest trap states in the system is reduced to $E_{A,T2,Cs5}$= 195 meV as well as $E_{A,T2,Rb5Cs5}$= 205 meV (T2). Furthermore, an additional but small contribution of energetically shallow trap states with a depth of $E_{A,T3,Cs5}$ = 105 meV and $E_{A,T3,Rb5Cs5}$ = 70 meV appears in both Cs-containing films (T3).

From the TSC measurements, it is not possible to deduce if the trap states found in Cs5 or Rb5Cs5 are also present in the broad background of deeper trap states in the FAMA or Rb5 samples. Neither can their polarity be determined. However, we note that Cs either leads to the removal of detrimental deep traps or a shift of these traps closer to the conduction or valence band in the FAMA perovskite. Contrarily, Rb has almost no influence on either the density or the energetic distribution of those trap states. Our TRMC results support the possibility of a reduced number of traps within the perovksite layer upon Cs-addition. We judge the lower number of deeper traps

to be beneficial for solar cell performance, as the recombination mediated by these states is reduced, which is in agreement with the improved V_{oc} of the Cs5 and Rb5Cs5 devices.

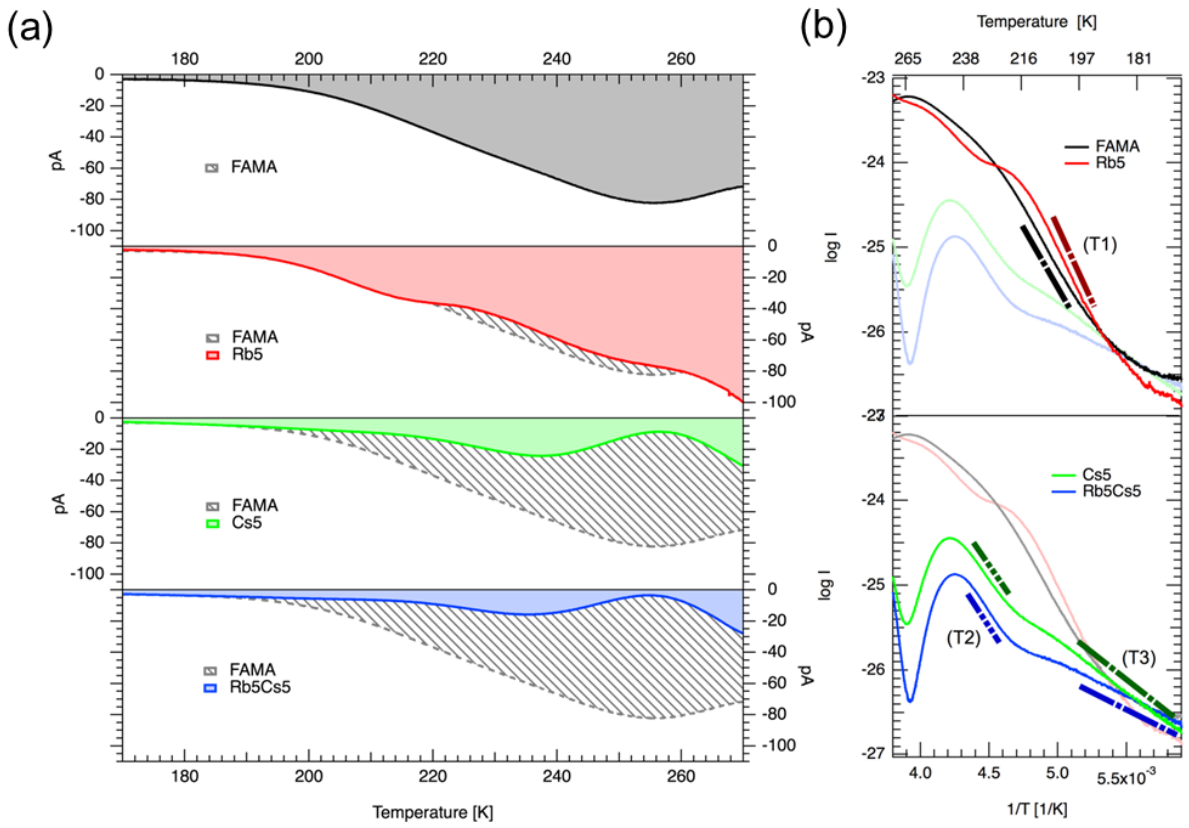

Figure 4. a) TSC spectra of full solar cells employing FAMA, Cs5, Rb5 or Rb5Cs5 as the active perovskite layer. The hatched areas indicate the difference in the amount of traps in the respective perovskite solar cell compared to the FAMA-based device. b) Arrhenius plots of the TSC spectra in the relevant temperature regions to estimate the activation energy of the trap states. The bars labeled T1, T2 and T3 mark the data range used for fitting according to the initial rise method.

Finally, not only the energetic depth of the trap states is changed by the inorganic cation additive, but also the overall signal height, which is associated with the trap density. We note here that

the trap density values deduced from TSC measurements constitute a lower limit, as charge carriers may also recombine after being released from the trap state during the measurement. Only those charge carriers released from the trap state and subsequently extracted at external contacts are detected by the TSC method. In order to estimate the lower limit of trap densities $N_{T,TSC}$ in the different perovskite solar cells, the TSC signal can be integrated over the elapsed time according to the equation:[31]

$$\int_{signal} I_{TSC} dt \leq e N_{T,TSC} Vol \qquad (3)$$

where *e* is the elementary charge and *Vol* is the volume of the perovskite layer. The estimated lower limits of trap densities are presented in **Table 3**, where the integral was calculated for the timespan of the temperature rise from 170–270 K.

Table 3. Activation energies of trap states and trap densities in perovskite solar cells determined by TSC measurements.

Device	$E_{A,T1}$ [meV]	$E_{A,T2}$ [meV]	$E_{A,T3}$ [meV]	$N_{T,TSC}$ [cm^{-3}]
FAMA	248	-	-	7.3×10^{16}
Rb5	283	-	-	7.2×10^{16}
Cs5	-	195	105	2.2×10^{16}
Rb5Cs5	-	205	70	1.6×10^{16}

Our results show that the addition of Cs removes a considerable amount of trap states from the system ($N_{T,TSC}$= 2.2×10^{16} cm^{-3}) as compared with FAMA devices ($N_{T,TSC}$= 7.3×10^{16} cm^{-3}), which is not the case if only Rb is introduced ($N_{T,\ TSC}$= 7.2×10^{16} cm^{-3}). With a trap density of $N_{T,TSC}$= 1.6×10^{16} cm^{-3}, the combination of both Rb and Cs shows the lowest value of all devices,

corresponding to an almost 80% lower number of trap states in the Rb5Cs5 system compared to pure FAMA.

We point out that the TSC method does not directly indicate whether the detected traps are located in the bulk, at grain boundaries or at an interface with the transport layers. However, our TRMC measurements show the same trend as TSC in trap density reduction, while solely probing the local properties of the perovskite absorber layer. Combining these experimental results allows us to deduce that Cs significantly reduces the trap denstity in the bulk or in the grain boundaries of the perovskite material. We tentatively assign the discrepancy between the overall absolute values for the trap densities extracted from these two techniques to the presence of the charge transport layers and associated interfacial effects being additionally measured in TSC, which is under further investigation. However, since all solar cells probed by the TSC technique were fabricated with the same contact materials, it is reasonable to assume that the extracted trends from TSC can indeed be assigned to the different perovskite materials employed.

3. Discussion

The addition of Cs and/or Rb salts to the perovskite precursor solution has a strong impact on the film's crystallization behavior, confirming previous reports in literature.[1-3] One possible explanation for the change in the perovskite crystallization process is the lower solubility of rubidium and particularly cesium halides in DMF, compared to the perovskite precursors FAI and MABr.[10, 32-34] This may lead to the rapid formation of crystal nuclei already during the spin-coating procedure. In the presence of the inorganic cation additives, the formation of potentially

defect-prone intermediate crystal phases such as mixed-dimensional hexagonal polytypes or DMSO-complexes is circumvented.[2, 35] In particular, Cs initiates the prompt formation of the quasi-cubic perovskite crystal phase, evident in the corresponding XRD peaks and the dark-brown color of non-annealed Cs5 and Rb5Cs5 films (Figure S13). As a result, higher XRD peak intensities for the perovskite phase are found in Rb5, Cs5 and Rb5Cs5 films after annealing (Figure S14) which indicates higher crystalline order than in pure FAMA. Besides improving the perovskite crystallization mechanism, the actual incorporation of the inorganic cations into the perovskite lattice probably plays a critical role in affecting the charge transport and trap landscape of the metal halide perovskite.

Our complementary probing techniques reveal that the addition of Cs barely affects the charge carrier mobility, but considerably reduces the trap density and the effective second order recombination rate in the metal halide perovskite, which likely leads to the higher V_{oc} and therefore higher performance found in Cs containing devices. Interestingly, the local, contactless TRMC technique on bare perovskite films showed the same trends for the trap density as the TSC measurements obtained with complete devices. Due to the excellent consistency between the TRMC and the TSC results, we assign the observed changes induced by Cs-addition rather to the bulk or boundaries of the perovskite crystals than solely to effects at the perovskite/transport layer interfaces.

By contrast, the Rb-addition leads to increased charge carrier mobilities in Rb5 compared to FAMA, which may be related to improved charge transport across the perovskite grain boundaries. However, with the high and balanced mobilities found in FAMA films, efficient

charge collection and injection should be enabled, and mobility is unlikely to be the limiting factor for charge diffusion. Our results show that Rb has only a marginal effect on the trap landscape of the entire perovskite device. Since we only found a minor improvement in Rb5 device performance compared to FAMA, we suggest that in our samples it is the amount and nature of trap states inside the perovskite that mainly limits efficiency. Despite the minimal impact of Rb on the PCE values obtained from *J–V* curves, we nonetheless observed improved power output stability and reduced *J–V* hysteresis in Rb containing devices (see Figure 1 and Figure S1). In the literature, the reduction of hysteresis in quadruple cation mixtures has been assigned to a lower defect density and thus a lower trap density within the perovskite crystals compared to triple cation mixtures without Rb.[12] Contrary to this, we see a reduced hysteresis in the case of Rb5Cs5 devices compared to Cs5 devices, where our TSC and TRMC results indicate rather similar trap densities. Therefore, it is unlikely that hysteresis is suppressed simply because of a reduction of traps in the bulk perovskite material. Alternatively, it has been suggested that the Rb-induced formation of larger perovskite crystals with fewer grain boundaries reduces ionic migration along grain boundaries, hence diminishing hysteresis.[12, 36] However, our SEM images reveal comparable grain sizes for the Cs5 and Rb5Cs5 samples examined here (Figure S10), ruling out the density of perovskite grain boundaries being the main reason for the reduced *J–V* hysteresis.

Instead, our study tallies with several recent publications and the combined results point to the following explanation: We recently found that 5–10% Cs cations can be incorporated into the FAMA perovskite structure, while the same amount of Rb cations does not form part of the perovskite lattice due to its unsuitably small ionic radius. As a result, the addition of 5–10% Rb mainly leads to the formation of non-perovskite side-phases such as $RbPb(I_{1-x}Br_x)_3$.[16] These

findings are in excellent agreement with the most recent solid state NMR results on multiple-cation perovskites reported by Kubicki *et al.*[37] The fundamentally different effects of Cs and Rb cations on the FAMA perovskite crystal lattice (**Figure 5**) may explain their different impact on the perovskite's trap landscape, charge transport properties, device performance and hysteresis.

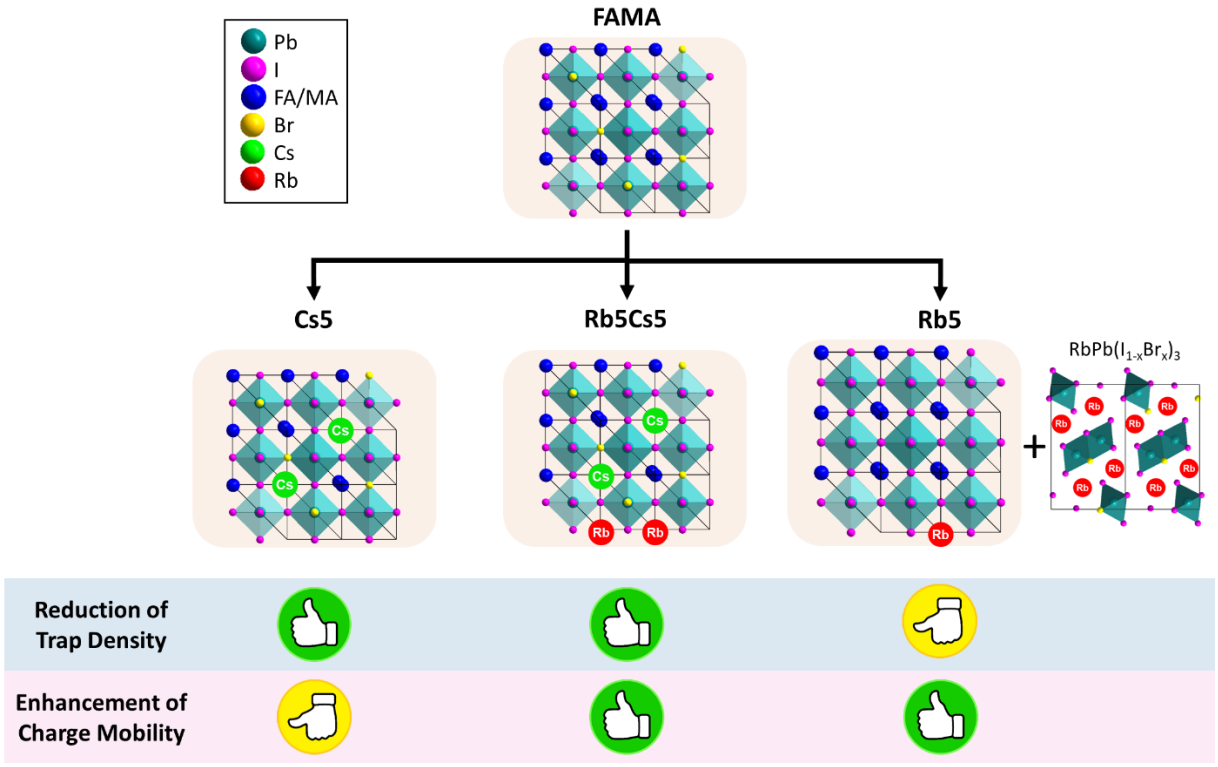

Figure 5. Schematic illustration of the hypothesized distribution of the inorganic cation additives within the perovskite crystal and the effect of Cs/Rb addition on the reduction of trap density and enhancement of charge carrier mobility within the perovskite layer.

Furthermore, charge accumulation and surface recombination at the interfaces between the perovskite and the selective charge transport layers have been shown to strongly affect *J*–*V* hysteresis.[38] We hypothesize that Rb could have an influence on these interfaces, as it is not

fully incorporated into the perovskite crystal structure itself. To obtain information about the distribution of the cation additives within the perovskite layer, we performed Time-of-Flight Secondary Ion Mass Spectrometry (ToF-SIMS) measurements on the different perovskite films deposited on TiO_2/FTO-glass substrates (Figure S15). Indeed, the depth profile for the Rb5 sample shows a clear accumulation of Rb^+ species at the TiO_2 interface, while Cs^+ is very homogeneously distributed within the Cs5 film. In Rb5Cs5, the presence of Cs^+ leads to a more even distribution of Rb^+ which is in accordance with work by Philippe *et al.*, only a slight Rb-enrichment still occurs between the perovskite layer and the substrate.[39] Our ToF-SIMS results are in excellent agreement with recent work by Albadri *et al.*, who reported that surface passivation effects of Rb give rise to reduced recombination at the TiO_2/perovskite interface compared to triple cation systems without Rb.[40] We believe that the enrichment of Rb cations at the electron transport layer interface is possibly related to a reduction of surface recombination in the vicinity of the electron transporting layer, which in turn affects device hysteresis and power output stability. Furthermore, Guo *et al.* predicted by first-principle calculations that an accumulation of the Rb-additives at the surface of perovskite crystals is energetically favored over their incorporation into the inner atomic layers, possibly giving rise to altered properties of the grain boundaries between the crystals.[41] Consequently, this might not only explain the difference in charge carrier mobilities we identified in our ToF and TRMC experiments, but also offers an additional explanantion for the change in *J–V* hysteresis. We are currently carrying out investigations to further elucidate this matter.

4. Conclusions

By combining three complementary characterization techniques – ToF, TRMC and TSC measurements – we could establish the influence of Cs- and Rb-addition on the charge carrier mobilities, recombination rates and trap states of state-of-the-art multiple-cation perovskites. We found that Rb-addition leads to increased charge carrier mobilities in Rb5 compared to FAMA, but has only a marginal effect on the trap landscape of the perovskite layer. This results in a minor improvement in device performance of Rb5 compared to the FAMA control device. By contrast, Cs-incorporation significantly reduces the number and the depth of trap states in the perovskite crystals. However, Cs has barely an effect on the charge carrier mobility. The observed reduction in trap density is in excellent agreement with the boost in V_{oc} and FF for Cs-containing devices compared to FAMA. By combining Cs and Rb in quadruple cation (Rb-Cs-FA-MA) perovskite mixtures, we observe the highest mobility and the lowest trap density, resulting in solar cells with the highest stabilized power output. We conclude that in the examined multiple-cation perovskite solar cells, the bottleneck for device efficiency is mainly the amount and the nature of the traps rather than insufficient charge carrier mobility in the perovskite.

5. Experimental Section

Materials: FAI and MABr were purchased from Dyesol. PbI_2 and $PbBr_2$ (99%) were purchased from TCI. CsI (99.9%) and all anhydrous solvents (DMSO, DMF, chlorobenzene) were purchased from Sigma-Aldrich and RbI from abcr GmbH. All chemicals were used without further purification.

Perovskite Film Fabrication: Perovskite precursor solutions for FAMA, Cs5, Rb5 and Rb5Cs5 were fabricated according to a previous report.[1, 16] Details on the exact solution composition can be found in the Supporting Information. 75 µL of the perovskite precursor solution was spin-coated inside a nitrogen-filled glovebox at 1000 rpm and 4000 rpm for 10 s and 30 s, respectively. Approximately 20 s before the end of spinning, 500 µL of chlorobenzene was added to the film. The perovskite film formation was completed by annealing at 100 °C for 60 min on a hotplate.

Device Fabrication: Fluorine-doped tin oxide (FTO) coated glass substrates (7 Ω/sq) were patterned by etching with zinc powder and 3 M HCl solution and successively cleaned with deionized water, a 2% Hellmanex detergent solution, ethanol and finally treated with oxygen plasma for 5 min. A compact TiO_2 layer was deposited as hole blocking layer on the substrate *via* a sol-gel approach. A mixture of 2 M HCl (35 µL) and anhydrous isopropanol (2.53 mL) was added dropwise to a solution of 370 µL titanium(IV) isopropoxide (Sigma-Aldrich) in isopropanol (2.53 mL) under vigorous stirring. The TiO_x solution was spin-coated dynamically onto the FTO substrates at 2000 rpm for 45 s, followed by annealing in air at 150 °C for 10 min and subsequently at 500 °C for 45 min. Alternatively, 10–15 nm compact SnO_x electron transport layers were prepared by atomic layer deposition (ALD) on FTO-coated glass substrates which were patterned and cleaned as in the TiO_2 preparation. Tetrakis (dimethylaminotin) (IV) (TDMASn, Strem, 99.99%) was used as a tin precursor. The deposition was conducted at 118 ^oC with a base pressure of 5 mbar in a Picosun R-200 Advanced ALD reactor. The tin precursor was held at 75 ^oC during depositions. Ozone gas was produced by an ozone generator (INUSA AC2025). Nitrogen (99.999%, Air Liquide) was used as the carrier and purge gas with a flow rate of 50 sccm per precursor line. The growth rate was determined via spectroscopic

ellipsometry on Si(100) witness substrates. A Cauchy model was used for the tin oxide layer and the growth rate was 0.69 Å per cycle. After the deposition of the electron transporting layer and the perovskite layer, a 2,2',7,7'-tetrakis-(*N,N*-di-*p*-methoxyphenyl-amine)-9,9'-spirobifluorene (spiro-OMeTAD) hole transporter layer was applied. 1 mL of a solution of spiro-OMeTAD (Borun Chemicals, 99.8%) in anhydrous chlorobenzene (75 mg/mL) was doped with 10 µL 4-*tert*-butylpyridine (Sigma-Aldrich, 96%) and 30 µL of a 170 mg/mL lithium bis(trifluoromethane)sulfonimidate (Li-TFSI) (Sigma-Aldrich, 99.95%) solution in acetonitrile (Sigma-Aldrich, anhydrous) and deposited by spin-coating at 1500 rpm for 40 s and then 2000 rpm for 5 s. After storing the samples overnight in air at 25% relative humidity, 40 nm Au was deposited through a patterned shadow mask by thermal evaporation at 8×10^{-7} mbar to form the back electrode.

Thin Film Characterization: X-ray diffraction (XRD) measurements of thin films were performed with a Bruker D8 Discover X-ray diffractometer operating at 40 kV and 30 mA, employing Ni-filtered Cu $K_{\alpha 1}$ radiation (λ = 1.5406 Å) and a position-sensitive LynxEye detector. SEM images were recorded with a FEI Helios Nanolab G3 UC DualBeam scanning electron microscope. UV-VIS absorption spectra were recorded with a Perkin-Elmer Lambda 1050 spectrophotometer equipped with an integrated sphere. The thin films were placed under an angle of 10° inside the sphere to detect the total fraction of reflected and transmitted photons, from which the fraction of absorbed photons was determined as a function of wavelength. Time-resolved PL spectroscopy was performed with a Picoquant Fluotime 300 spectrofluorometer, using an excitation wavelength at 510 nm and by monitoring the PL emission maximum around 780 nm. The depth profiles of perovskite films on TiO_2/FTO-glass substrates were measured with a ToF-

SIMS 5 setup from ION-TOF GmbH. Pulsed primary ions from a 30 keV Bi^+ liquid-metal ion gun were used as an analytical source, and a 10 keV O_2-cluster source was used as a sputtering ion source. The ToF-SIMS analysis was done on a 100 × 100 µm area inside the 300 × 300 µm sputtering crater.

Current-Voltage Characterization: J-V curves were recorded under ambient conditions using a Newport OrielSol 2A solar simulator with a Keithley 2400 source meter under simulated AM1.5G sunlight, with an incident power of 100 mW cm^{-2}, calibrated with a Fraunhofer ISE certified silicon cell (KG5-filtered). The active area of the solar cells was defined with a square metal aperture mask of 0.0831 cm^2. After pre-biasing the device at 1.5 V for 5 s under illumination, *J-V* curves were recorded by scanning the input bias from 1.5 V to 0 V (reverse scan) and then from 0 V to 1.5 V (forward scan) at a scan rate of 0.1–0.2 V s^{-1}. For statistical evaluation, the photovoltaic parameters were extracted from the *J–V* curve showing the higher PCE value. The stabilized power output was measured by tracking the photocurrent at the maximum power point without pre-biasing the device.

Time-of-Flight measurements: Laterally contacted perovskite films with inter-electrode distances of 22–80 µm were fabricated by evaporating gold through a shadow mask. The samples were illuminated from the semi-transparent glass/Au side using pulsed laser excitation at a wavelength of 510 nm with a repetition rate of 20 Hz and a pulse length of 7 ns. The charge carriers were generated close to one Au contact by focusing the laser through an extra-long working distance microscope objective (spot size approximately 2 µm). By applying a constant external electric field at the electrodes only for the short measurement interval of a few hundred milliseconds to

avoid effects due to ion migration, a current flow is created, leading to the respective ToF photocurrent transient. The generated *J–t* profiles were amplified and converted before being recorded with a fast oscilloscope (see Supporting Information for further details).

Time-Resolved Microwave Conductivity measurements: TRMC experiments were performed on perovskite films on quartz substrates according to a previously reported procedure.[24] The change in microwave power (probe frequency: 8.5 GHz) was monitored after pulsed excitation of the sample at 650 nm (repetition rate: 10 Hz). Neutral density filters were used to vary the intensity of the incident light. Further experimental details, the employed kinetic model and information about the fitting process can be found in the Supporting Information.

Thermally Stimulated Current measurements: TSC measurements were conducted in a closed cycle He cryostat, with Helium as a contact gas for thermal coupling. To avoid any atmospheric exposure, solar cell samples were transferred via an integrated sample lock system from a glove box to the cryostat. Trap filling was achieved via illumination with an LED array for 10 min. After a dwell time of 10 min in the darkness, the sample was heated up to 300 K at a constant rate of 3 K min^{-1}. The TSC signal of the sample was detected by a Sub-Femtoamp Remote Source Meter (Keithley 6430) without the application of a bias voltage.

Supporting Information

Supporting Information is available from the Wiley Online Library or from the author.

Acknowledgements

The authors thank Dr. Steffen Schmidt from the LMU Munich for the SEM images. This project was financed by grants from the Federal Ministry of Education and Research (BMBF) under the project ID 03SF0516B and project ID 03SF0514A/B. The authors acknowledge funding from the Bavarian Collaborative Research Program “Solar Technologies Go Hybrid” (SolTech), the Center for NanoScience (CeNS), and the DFG Excellence Cluster “Nanosystems Initiative Munich” (NIM). E.M.H and T.S. thank the Netherlands Organisation for Scientific Research (NWO) for funding. A.B. and V.D. work at the ZAE Bayern, which is financed by the Bavarian Ministry of Economic Affairs and Media, Energy and Technology. P.R. acknowledges the DFG for funding in the framework of the GRK 2112. M.F.A. acknowledges the Scientific and Technological Research Council of Turkey. A.G.H. acknowledges funding by the Fonds der chemischen Industrie.

The authors Y. H., E.M.H. and P. R. contributed equally to this work.

Received:
Revised:
Published online:

Conflict of Interest

The authors declare no conflict of interest.

References

[1] M. Saliba, T. Matsui, K. Domanski, J.-Y. Seo, A. Ummadisingu, S. M. Zakeeruddin, J.-P. Correa-Baena, W. R. Tress, A. Abate, A. Hagfeldt, M. Grätzel, *Science* **2016**, *354*, 206.
[2] M. Saliba, T. Matsui, J.-Y. Seo, K. Domanski, J.-P. Correa-Baena, M. K. Nazeeruddin, S. M. Zakeeruddin, W. Tress, A. Abate, A. Hagfeldt, M. Gratzel, *Energy. Environ. Sci.* **2016**, *9*, 1989.
[3] J.-W. Lee, D.-H. Kim, H.-S. Kim, S.-W. Seo, S. M. Cho, N.-G. Park, *Adv. Energy Mater.* **2015**, *5*, 1501310.
[4] Z. Li, M. Yang, J.-S. Park, S.-H. Wei, J. J. Berry, K. Zhu, *Chem. Mater.* **2016**, *28*, 284.
[5] T. Duong, H. K. Mulmudi, H. Shen, Y. Wu, C. Barugkin, Y. O. Mayon, H. T. Nguyen, D. Macdonald, J. Peng, M. Lockrey, W. Li, Y.-B. Cheng, T. P. White, K. Weber, K. Catchpole, *Nano Energy* **2016**, *30*, 330.
[6] C. Yi, J. Luo, S. Meloni, A. Boziki, N. Ashari-Astani, C. Gratzel, S. M. Zakeeruddin, U. Rothlisberger, M. Gratzel, *Energy. Environ. Sci.* **2016**, *9*, 656.
[7] T. Liu, Y. Zong, Y. Zhou, M. Yang, Z. Li, O. S. Game, K. Zhu, R. Zhu, Q. Gong, N. P. Padture, *Chem. Mater.* **2017**, *29*, 3246.
[8] A. Binek, F. C. Hanusch, P. Docampo, T. Bein, *J. Phys. Chem. Lett.* **2015**, *6*, 1249.
[9] L.-Q. Xie, L. Chen, Z.-A. Nan, H.-X. Lin, T. Wang, D.-P. Zhan, J.-W. Yan, B.-W. Mao, Z.-Q. Tian, *J. Am. Chem. Soc.* **2017**, *139*, 3320.
[10] D. P. McMeekin, G. Sadoughi, W. Rehman, G. E. Eperon, M. Saliba, M. T. Hörantner, A. Haghighirad, N. Sakai, L. Korte, B. Rech, M. B. Johnston, L. M. Herz, H. J. Snaith, *Science* **2016**, *351*, 151.
[11] Y. Chang, L. Wang, J. Zhang, Z. Zhou, C. Li, B. Chen, L. Etgar, G. Cui, S. Pang, *J. Mater. Chem. A* **2017**, *5*, 4803.
[12] T. Duong, Y. Wu, H. Shen, J. Peng, X. Fu, D. Jacobs, E.-C. Wang, T. C. Kho, K. C. Fong, M. Stocks, E. Franklin, A. Blakers, N. Zin, K. McIntosh, W. Li, Y.-B. Cheng, T. P. White, K. Weber, K. Catchpole, *Adv. Energy Mater.* **2017**, *7*, 1700228.
[13] D. P. McMeekin, Z. Wang, W. Rehman, F. Pulvirenti, J. B. Patel, N. K. Noel, M. B. Johnston, S. R. Marder, L. M. Herz, H. J. Snaith, *Adv. Mater.* **2017**, 1607039.
[14] Y. H. Park, I. Jeong, S. Bae, H. J. Son, P. Lee, J. Lee, C.-H. Lee, M. J. Ko, *Adv. Funct. Mater.* **2017**, 1605988.
[15] M. Zhang, J. S. Yun, Q. Ma, J. Zheng, C. F. J. Lau, X. Deng, J. Kim, D. Kim, J. Seidel, M. A. Green, S. Huang, A. W. Y. Ho-Baillie, *ACS Energy Lett.* **2017**, 438.
[16] Y. Hu, M. F. Aygüler, M. L. Petrus, T. Bein, P. Docampo, *ACS Energy Lett.* **2017**, 2212.
[17] M. L. Petrus, Y. Hu, D. Moia, P. Calado, A. M. A. Leguy, P. R. F. Barnes, P. Docampo, *ChemSusChem* **2016**, *9*, 2699.
[18] Q. Chen, H. Zhou, T.-B. Song, S. Luo, Z. Hong, H.-S. Duan, L. Dou, Y. Liu, Y. Yang, *Nano Lett.* **2014**, *14*, 4158.
[19] C. Roldan-Carmona, P. Gratia, I. Zimmermann, G. Grancini, P. Gao, M. Graetzel, M. K. Nazeeruddin, *Energy. Environ. Sci.* **2015**, *8*, 3550.
[20] I. Grill, K. Handloser, F. C. Hanusch, N. Giesbrecht, T. Bein, P. Docampo, M. Handloser, A. Hartschuh, *Sol. Energy Mater. Sol. Cells* **2017**, *166*, 269.
[21] H. D. Kim, H. Ohkita, H. Benten, S. Ito, *Adv. Mater.* **2015**.
[22] E. M. Hutter, G. E. Eperon, S. D. Stranks, T. J. Savenije, *J. Phys. Chem. Lett.* **2015**, *6*, 3082.

[23] S. D. Stranks, V. M. Burlakov, T. Leijtens, J. M. Ball, A. Goriely, H. J. Snaith, *Physical Review Applied* **2014**, *2*, 034007.
[24] E. M. Hutter, J.-J. Hofman, M. L. Petrus, M. Moes, R. D. Abellón, P. Docampo, T. J. Savenije, *Adv. Energy Mater.* **2017**, *7*, 1602349.
[25] J. M. Richter, M. Abdi-Jalebi, A. Sadhanala, M. Tabachnyk, J. P. H. Rivett, L. M. Pazos-Outón, K. C. Gödel, M. Price, F. Deschler, R. H. Friend, **2016**, *7*, 13941.
[26] E. M. Hutter, M. C. Gelvez-Rueda, A. Osherov, V. Bulovic, F. C. Grozema, S. D. Stranks, T. J. Savenije, *Nat Mater* **2017**, *16*, 115.
[27] L. M. Pazos-Outón, M. Szumilo, R. Lamboll, J. M. Richter, M. Crespo-Quesada, M. Abdi-Jalebi, H. J. Beeson, M. Vrućinić, M. Alsari, H. J. Snaith, B. Ehrler, R. H. Friend, F. Deschler, *Science* **2016**, *351*, 1430.
[28] A. Baumann, S. Väth, P. Rieder, M. C. Heiber, K. Tvingstedt, V. Dyakonov, *J. Phys. Chem. Lett.* **2015**, *6*, 2350.
[29] G. F. J. Garlick, A. F. Gibson, *Proceedings of the Physical Society* **1948**, *60*, 574.
[30] W. Graupner, G. Leditzky, G. Leising, U. Scherf, *Physical Review B* **1996**, *54*, 7610.
[31] A. Kadashchuk, R. Schmechel, H. v. Seggern, U. Scherf, A. Vakhnin, *J. Appl. Phys.* **2005**, *98*, 024101.
[32] R. Alexander, E. C. F. Ko, Y. C. Mac, A. J. Parker, *J. Am. Chem. Soc.* **1967**, *89*, 3703.
[33] R. Hamaguchi, M. Yoshizawa-Fujita, T. Miyasaka, H. Kunugita, K. Ema, Y. Takeoka, M. Rikukawa, *Chem. Commun.* **2017**, *53*, 4366.
[34] R. E. Beal, D. J. Slotcavage, T. Leijtens, A. R. Bowring, R. A. Belisle, W. H. Nguyen, G. F. Burkhard, E. T. Hoke, M. D. McGehee, *J. Phys. Chem. Lett.* **2016**, *7*, 746.
[35] P. Gratia, I. Zimmermann, P. Schouwink, J.-H. Yum, J.-N. Audinot, K. Sivula, T. Wirtz, M. K. Nazeeruddin, *ACS Energy Lett.* **2017**, 2686.
[36] H.-S. Kim, N.-G. Park, *J. Phys. Chem. Lett.* **2014**, *5*, 2927.
[37] D. J. Kubicki, D. Prochowicz, A. Hofstetter, S. M. Zakeeruddin, M. Grätzel, L. Emsley, *J. Am. Chem. Soc.* **2017**, *139*, 14173.
[38] P. Calado, A. M. Telford, D. Bryant, X. Li, J. Nelson, B. C. O'Regan, P. R. F. Barnes, *Nat. Commun.* **2016**, *7*, 13831.
[39] B. Philippe, M. Saliba, J.-P. Correa-Baena, U. B. Cappel, S.-H. Turren-Cruz, M. Grätzel, A. Hagfeldt, H. Rensmo, *Chem. Mater.* **2017**, *29*, 3589.
[40] A. Albadri, P. Yadav, M. H. Alotaibi, N. Arora, A. Y. Alyamani, H. A. H. Albrithen, M. I. Dar, S. M. Zakeeruddin, M. Grätzel, *J. Phys. Chem. C* **2017**.
[41] Y. Guo, C. Li, X. Li, Y. Niu, S. Hou, F. Wang, *J. Phys. Chem. C* **2017**, *121*, 12711.

Table of contents entry: Time-Resolved Microwave Conductivity, Time-of-Flight and Thermally Stimulated Current measurements reveal that Cs reduces the trap density in hybrid lead halide perovskites. Rb additives enhance the charge carrier mobility, but show minor effects on the trap

landscape. The increase in open-circuit voltage in multiple-cation perovskite solar cells can be related to a reduced trap density through Cs-incorporation.

Keywords: perovskite solar cell, inorganic cations, trap density, charge carrier mobility, charge recombination

Yinghong Hu,[1] Eline M. Hutter,[2] Philipp Rieder,[3] Irene Grill,[1] Jonas Hanisch,[4] Meltem F. Aygüler,[1] Alexander G. Hufnagel,[1] Matthias Handloser,[5] Erik Ahlswede,[4] Thomas Bein,[1] Achim Hartschuh,[1] Kristofer Tvingstedt,[3] Vladimir Dyakonov,[3] Andreas Baumann,[6,] Tom J. Savenije,[2,*] Michiel L. Petrus,[1,*] Pablo Docampo.[7,*]*

Understanding the Role of Cesium and Rubidium Additives in Perovskite Solar Cells: Trap States, Charge Transport and Recombination